

Disorder induced local density of states oscillations on narrow Ag(111) terraces

Karina Morgenstern and Karl-Heinz Rieder

Institut für Experimentalphysik, FB Physik, Freie Universität Berlin, Arnimallee 14, D-14195 Berlin, Germany

Gregory A. Fiete

Kavli Institute for Theoretical Physics, University of California, Santa Barbara, CA 93106, USA

(Dated: February 2, 2008)

The local density of states of Ag(111) has been probed in detail on disordered terraces of varying width by dI/dV-mapping with a scanning tunneling microscope at low temperatures. Apparent shifts of the bottom of the surface-state band edge from terrace induced confinement are observed. Disordered terraces show interesting contrast reversals in the dI/dV maps as a function of tip-sample voltage polarity with details that depend on the average width of the terrace and the particular edge profile. In contrast to perfect terraces with straight edges, standing wave patterns are observed parallel to the step edges, i.e. in the non-confined direction. Scattering calculations based on the Ag(111) surface states reproduce these spatial oscillations and all the qualitative features of the standing wave patterns, including the polarity-dependent contrast reversals.

PACS numbers: 73.20.At, 73.20.-r, 68.37.Ef

I. INTRODUCTION

The fcc(111) surfaces of noble metals exhibit a large sp-band gap in the projected bulk band structure along the Γ -L line.^{1,2} These gaps reach down below the Fermi energy at the center of the surface Brillouin zone and support an occupied free electron surface-state.^{3,4} Electrons occupying these Shockley-type surface-states form a two-dimensional nearly free electron gas parallel to the surface.^{5,6,7} Electrons are confined to the vicinity of the top layer by the vacuum barrier on one side and a band gap in the bulk states on the other side.

Scanning tunneling microscopy (STM) and spectroscopy (STS) are particularly sensitive tools to study these surface-states that dominate in the zone between the tip and the surface.⁸ These techniques map the local electronic density of states (LDOS) in real space. STM has provided real space observation of electrons in surface-states and of their interactions with adsorbates,^{9,10} steps,^{9,10,11,12,13,14} and other structures^{9,10,15,16} in the form of standing wave patterns. These spatial oscillations are quantum mechanical interference patterns caused by the scattering of electrons in the two-dimensional electron gas from defects. The standing wave patterns contain information about the surface-state dispersion and they give insight into the interaction between surface-state electrons and scattering sites on the surface.^{9,10}

STS images of the local differential tip-surface conductance (called dI/dV maps) have been used to investigate how the surface-state interacts with a single straight atomic step^{17,18} and with a pair of adjacent straight steps.^{11,18} From the measurement of spatial oscillation periods normal to the step it was possible to extract Fermi wave vectors¹⁹ and complete energy dispersion curves.²⁰ Thus, the surface-state on clean, disorder-free systems is well characterized. However, growth and catalysis, which are both influenced by the electronic

structure of the surface,^{21,22,23} also occur on surfaces where disorder is present. In particular, the LDOS modulations on irregular step arrays²⁴ can have a dramatic impact on these processes. Therefore, it is important to understand and to be able to predict the electronic structure on disordered terraces of varying width limited by steps with irregular edges. A study of the electronic structure of such terraces is the focus of this paper.

In a recent publication, we have investigated the dependence of the LDOS near the Fermi-energy, E_F , on the width of terraces on Ag(111) at 7 K.²⁵ We showed that the *apparent* surface-state band minimum shifts monotonically towards the bulk E_F with decreasing terrace width leading to a depopulation at a mean terrace width $L = 3.2$ nm, in quantitative agreement with a Fabry-Pérot model with energy dependent finite asymmetric reflectivity of the step edges. In addition, a switch from confinement by terrace modulation to step modulation was observed at $\lambda_F/2$ ($L=3.7$ nm), half of the Fermi wavelength on an infinite terrace. This switch occurs on Cu(111) surfaces also at $\lambda_F/2$ as proven by photoemission.¹⁴

In this paper, we present STS data revealing spatial oscillations of the local density of states on Ag(111) for narrow disordered terraces of varying width up to 8.5 nm. Apparent band edge shifts of the surface-state onset (as reported in Ref. [25]) lead to conductance variations on terraces of different width at the same energy. A standing wave pattern also evolves parallel to the steps, i.e. in the non-confined direction. Its wavelength follows the dispersion relation of an electron in the clean, infinite surface-state. In order to understand the wave pattern, theoretical simulations based on scattering theory are performed for disordered terraces. These calculations successfully reproduce the observed oscillations parallel to the terraces as well as interesting tip-sample voltage polarity dependent effects.

This paper is organized in the following way. In Sec. II

we discuss the details of the experiment, including sample preparation, the types of measurements made, and the main features observed in the data. In Sec. III we discuss the theoretical model used to interpret the experiments and its assumptions. We also present the results of model calculations and discuss their connection with experiment. Finally, in Sec. IV we give the main conclusions of our work.

II. EXPERIMENT

A. Sample preparation and data acquisition

The experiments have been performed in ultrahigh vacuum with a low temperature scanning tunneling microscope that operates at temperatures between 6 and 300 K. The single crystalline Ag(111) surface is cleaned by sputtering and annealing cycles. The surface separates into large flat terraces and step bunches with an average terrace width of 4 nm.²⁴ In this paper, we investigate the spatial oscillations of the LDOS in these stepped regions. Measurements are performed at 7 K.

The topographic images are taken in constant current mode. dI/dV spectra are recorded with the lock-in technique; the ac tunnel current is driven by a 4 mV signal added to the junction bias with a frequency of 327.9 Hz, 381.8 Hz, or 738.1 Hz. Voltages are applied to the sample with respect to the tip. Thus, for a negative voltage the occupied side of the spectrum is probed. dI/dV maps are recorded simultaneously with the topographic images at the same voltage by recording the lock-in signal at each pixel. It is not possible to run the STM in constant height mode in imaging a step array of more than 1 nm change in height. Thus, the constant-current image recorded simultaneously with the dI/dV map is used for an adjustment in tip-sample separation. This leads to a superposition of the dI/dV signal with a variance in height at the step edges.

A dI/dV map of 256x256 pixels is recorded in about 80 minutes. Series of dI/dV maps therefore requires a high stability STM, which our system provides. Typically, the drift is less than 0.3 nm during a series of 10 dI/dV maps, i.e. 13 hours. Major drift problems arise from the increasing temperature at the end of helium evaporation. Therefore, measurement series on the same spot of the crystal are limited by the helium amount available in the bath cryostat.

B. Experimental results

For a defect-free terrace of ideally parallel steps, the surface-state electrons on each terrace are confined perpendicular to steps but are free parallel to them. Thus, the wave functions of surface-state electrons are separable, with standing waves normal to the steps and plane

waves parallel to the steps. This leads to a wave pattern *perpendicular* to the steps. Fig. 1a shows these well known spatial oscillation of the surface-state electrons *perpendicular* to pre-existing step edges on a large terrace of 51 nm in width. In addition, surface impurities act as point defects and lead to radial wave patterns centered on the impurities. At 32 mV the waves have the expected wavelength of $\lambda/2 = 3.5$ nm (See Ref. [20]). At 7 K five maxima are discernable already in the topographic image. Note the irregularities of the plane waves introduced by the natural deviation of the step edge position from a straight line.

The LDOS (as recorded in dI/dV spectra) displays a step-like function marking the sharp increase of differential conductivity around the surface-state band onset (Fig. 1b). Following Ref. [16], we measure the onset of the surface-state, $U_{on} = (U_{top} + U_{bot})/2$, and a width, $\Delta = U_{top} - U_{bot}$, of the onset by continuing the slope at the middle of the rise to the bottom and the top of the rise as indicated in Fig. 1b. The values of $U_{on} = -(68 \pm 4)$ meV and $\Delta = 8$ meV are in good agreement with earlier measurements.¹⁸

Confinement on narrow terraces leads to both a shift in energy of the surface-state related peak and a broadening of it.²⁵ Moreover, additional maxima develop. The example shown in Fig. 1c, taken on a terrace of 6.1 nm width, displays onsets at -53 meV and 32 meV with onset widths of $\Delta_{-53\text{meV}} = 23$ meV and $\Delta_{32\text{meV}} = 32$ meV, respectively. These two peaks correspond to the first two transverse modes of the surface state confined by the terrace edges.

The spectra vary for terraces of different width, but also for different positions on the same terrace (Fig. 2) with slight variations in apparent surface state onset energy and large variations in dI/dV intensity (Figs. 2b and c). In particular, close to the step edges, U_{bot} shifts to lower values influencing the onset value U_{on} (Fig. 2b). We have shown before that these variations close to the step edges are in accordance with a Fabry-Pérot model with the steps acting as finite, energy-dependent barriers, so this is no indication of a shift in energy.²⁵ As a consequence of strong scattering of the surface-state electrons by the step potential, the amplitude of the surface-state is smaller close to the step edges.²⁸ Thus, the peak intensity of dI/dV varies for the same terrace width depending on the distance from the step edges (Fig. 2c), being highest in the middle between the step edges for the first peak in dI/dV and showing two maxima for the second peak in dI/dV on the largest terrace. Only the widest terrace, the second one in Fig. 2a, shows two peaks in dI/dV.

The second peak arising in dI/dV due to local confinement on a single terrace should show a quadratic dependence of energy with terrace width according to a particle-in-a-box model for the simple case of infinitely high potential walls.²⁹ $E_{gnd} = \hbar^2 \pi^2 / 2m_{eff} L^2$, with m_{eff} the effective mass and L the terrace (confinement) width. The plot of the energy of the second peak relative to apparent surface-state onset vs. $1/L^2$ (Fig. 3) shows

indeed a linear dependence for terrace widths $> \lambda_F/2$, i.e. for those terraces where the Fabry-Pérot model is applicable.²⁵ From the prefactor of (6.371 ± 1.794) eV nm², we determine $m_{eff}^{terr} = (0.59 \pm 0.17) m_e$, which deviates from the effective mass of electrons in the surface-state band where $m_{eff} = 0.4m_e$.

To investigate spatial variations of the differential conductance in more detail, we have recorded dI/dV maps on these step arrays at different energies. Some examples are displayed in Figs. 4 to 7.

Below the onset of the surface-state, dI/dV maps display bright lines and spots on a continuous background (Fig. 4b to d). The bright lines correspond to the surface steps and are an artifact of the constant current scanning process (see above). The brightest spot in the dI/dV maps corresponds to an impurity at the step edge. It is visible in the topography as a protrusion imaged 20 pm higher than the surrounding step edge (Fig. 4a). This impurity can be used as a reference point to compensate for thermal drift. The two less bright spots are not visible in the topographic STM image in the contrast shown. Contrast enhancement shows them as protrusions of only 4 pm in height. We therefore attribute them to subsurface impurities.

With increasing voltage a difference in contrast develops between terraces of different width. For the broadest terrace “3”, there is a contrast switch from dark to bright between -50 mV and -40 mV (Fig. 4g to h). Narrower terraces switch contrast at voltages closer to E_F . The dependence of the switch in intensity on terrace width results from the different apparent surface-state onsets (see Fig. 2a). On the largest terrace “3” a wave pattern evolves *parallel* to the step edges. The wavelength of this wave pattern increases as the energy is lowered with respect to E_F . While a faint wave pattern discernable at -50 mV on terrace “3” (Fig. 4g) seems to originate from the subsurface impurity, the standing wave pattern at smaller energies is only perturbed by this impurity. The wave pattern does not originate from it.

There is no obvious correspondence between wave patterns on adjacent terraces. For example, at -30 meV (Fig. 4i) the distance between the uppermost maxima is different on terrace “3” and on terrace “4”. At -10 mV (Fig. 4k) the wave patterns on terraces “3” and “4” are phase shifted in the upper half of the image.

Fig. 5 compares the parallel wave pattern (-10 mV, Fig. 4k) to a pattern at opposite polarity, i.e. in the unoccupied region (+90 mV). At +90 mV the dominant wave pattern on terrace “3” runs perpendicular to the step edges, however, with contrast variations. Thus, perpendicular and parallel wave patterns are superimposed. Note that even at +90 meV the narrower terraces, e.g. “5”, show the parallel wave pattern only.

This superposition of parallel and perpendicular wave patterns becomes more pronounced on even broader terraces (Fig. 6). For the terrace “2” of 8.5 nm in width, the perpendicular wave pattern dominates at -38 mV (Fig. 6b). At +15 mV and +30 mV the contrast variation

along the perpendicular waves on the left half and on the right half of the terrace are independent of each other. This leads to an interference pattern at the middle of the terrace, which changes wavelength with energy (Fig. 6c to d). Note the differences of terrace “3” from the slightly narrower terrace “5” at +15 mV and +30 mV. Terrace “5” shows lower conductivity at its center than at its sides, while terrace “2” shows higher conductivity at its center compared to its sides. Also terraces “3” and “4” show wave patterns of opposite contrast.

The wavelength dependence on energy of the parallel wave pattern is investigated in more detail on the unoccupied side of the LDOS (Fig. 7). The standing wave pattern *parallel* to the surface steps on terrace “3” at positive polarity is contrast-reversed with respect to the standing wave pattern shown in Fig. 4. The dI/dV map at -30 mV (Fig. 7b) shows that this is an effect of the opposite polarity of the tip-sample voltage bias and not of the terrace width. Due to a subsurface impurity (see below) the wave pattern in the lower part of this image is less regular. Thus, we concentrate on the upper part of the image.

The average wavelength changes with bias voltage (Fig. 7m). For an ideal terrace with impenetrable edges, the isotropic free surface dispersion relation $E(\vec{k}) = E_0 + \frac{\hbar^2 k^2}{2m_{eff}}$, with $E_0 = -0.065$ eV, is modified by “confinement” due to the terrace structure,

$$E_n(k_{\parallel}) = E_0 + \frac{\hbar^2 \pi^2 n^2}{2m_{eff} L^2} + \frac{\hbar^2 k_{\parallel}^2}{2m_{eff}} , \quad (1)$$

where $k_{\parallel} \equiv 2\pi/\lambda_{\parallel}$ and n is the number of transverse modes. This equation predicts that for a fixed energy, narrower terraces with smaller width L will have a larger parallel wavelength, λ_{\parallel} . Examples of this effect can be seen in Figs. 4 to 7, although the oscillations in the narrower terraces are less regular for the narrower terrace. We attribute this to larger relative variations in width for fixed edge variations in the narrower terraces.

Furthermore, a quadratic variation of λ_{\parallel} with E is expected for a free electron dispersion (see Eq. (1)) provided no additional transverse modes are occupied over the energy range probed. Indeed, the data can be well fitted by $a(E - E_0)^{-1/2}$. We find $E_0 = -(67 \pm 5)$ meV, the same value as the bottom of the surface-state band determined from the surface-state onset on large terraces (see above) and from perpendicular wave patterns on large terraces.¹⁷ Also the wavelengths determined from the negative dI/dV maps of Fig. 4 fit a quadratic dispersion with $E_0 = -(68 \pm 19)$ meV. Fig. 7n displays the dispersion relation deduced from this measurement that reproduces the dispersion relation determined from perpendicular wave patterns.²⁰ Thus, parallel wave patterns originate also from the scattering of surface-state electrons.

III. THEORY

A. Model and approach

In this paper we are focused on understanding the role of disorder in the terrace edge profile on the observed modulations in the local density of states. Disorder in the edge profile breaks translational symmetry along the direction parallel to the terrace edges. This broken symmetry prevents a simple separation of the energy (and the wavefunctions) of the electrons into a parallel and transverse component, as was done in Eq. (1). In order to conveniently handle the broken translational symmetry another approach is needed. We chose to use a scattering theory²⁶ that has been quite successful in predicting the standing wave patterns in the LDOS observed with the STM around impurities and step edges on the surfaces of the noble metals that support surface-states.

The scattering theory given in Ref. [26] most naturally describes the scattering of electrons in the surface-state from point-like impurities (adatoms) where an s-wave scattering approximation can be made; scattering from an extended impurity, such as a terrace edge, requires some modification of the theory, which otherwise cannot directly describe scattering from an extended object. Fortunately, since the standing wave patterns we are interested in (those parallel to the terrace edges) are observed most clearly in the central portion of the terrace, we may make a simple approximation in the scattering theory for the terrace edge: We treat the terrace edge as a dense “row” of point (s-wave) scatterers. Far from the terrace edges (near the middle of the terrace, for example) the results will be indistinguishable from a terrace edge that is continuous. A “row” of atoms is expected to be a good approximation to the terrace edge provided the atoms that make up the wall are well within a wavelength (the wavelength of the surface-state electron) of each other and the distances probed are of the order of the separation of the atoms or larger. In the calculations described below our objective will be first to understand the qualitative features we can expect from scattering theory and second to compare as directly as possible with experiment. The latter requires determining the phase shift of a single atom (one of many that make up the terrace edge) so that the correct phase shift results for the edge as a whole. Since the input to the scattering theory is the wall profile, the dispersion of the surface-state electrons, and the s-wave scattering phase shift δ , the only free parameter we have in the theory is δ . We tune δ for a fixed wall profile and surface-state dispersion to reproduce the experimental dI/dV vs. V spectra at the center of the terrace. Once δ is optimized in this way, we computed the dI/dV image maps (at a fixed voltage) over all positions using this value and the exact edge profile of the terraces.

B. Theoretical calculations

1. Model calculation for qualitative effects

To understand the qualitative effects we expect from a scattering theory approach to the LDOS modulations from disordered terraces, we first carried out calculations on a single terrace with perfectly straight walls and then added in increasing amounts of disorder. The terraces were modeled by placing 21 point (s-wave) scatterers at a distance of $\lambda_F/4$ along the terrace edge. See Fig. 8.

The dI/dV maps were computed using the surface-state dispersion $E(\vec{k}) = E_0 + \frac{\hbar^2 k^2}{2m_{eff}}$. (Confinement effects that do not cause an apparent shift in the surface-state band minimum are captured automatically by electron scattering from the terrace “edges”.) An approximation to the “constant current” condition used in the experiment (while simultaneously acquiring topographic and dI/dV maps) is achieved by calculating

$$\left[\frac{dI}{dV}(eV) \right]_{\text{meas}} \equiv \left[\frac{dI}{dV}(eV) \right]_{\text{calc}} - \langle \left[\frac{dI}{dV} \right]_{\text{calc}} \rangle \quad (2)$$

where $\langle \left[\frac{dI}{dV} \right]_{\text{calc}} \rangle = \int_0^{eV} d\epsilon \left[\frac{dI}{dV}(\epsilon) \right]_{\text{calc}} (eV)^{-1}$. This procedure correctly reproduces brightness variations in dI/dV maps simultaneously taken with topographic maps.²⁷

In these initial model calculations, each scatterer is assumed to have a phase shift of $\pi/2$. This value turns out to be almost “universal” for adatoms on the surfaces of noble metals²⁶ so we take it as a starting point; later we will find a different value matches the experiments better when we attempt to make a direct, quantitative comparison between theory and experiment. The initial choice of $\pi/2$ is arbitrary and does not affect any of the qualitative conclusions reached from the calculations presented in Figs. 8 and 9. While this value works well for single adatoms, the physics of scattering from a terrace edge is very different from the physics of scattering from an isolated atom, and this is why the best phase shift for the terrace edge atom differs from $\pi/2$.

Fig. 8a shows the calculated $[dI/dV]_{\text{calc}}$ map for a trough of $5\lambda_F$ in length and $\lambda_F/4$ in width limited by 21 point scatterers on each side. While the perpendicular standing wave pattern outside the trough is clearly visible, its narrowness inhibits a similar wave pattern within the trough. It is too small to support even half of a Fermi-wavelength. The introduction of an arbitrary defect in one of the terrace walls leads to standing waves parallel to the rows of atoms with the same wavelength $\lambda_F/2$ as the perpendicular wave outside the trough (Fig. 8b). Note the faint signs of oscillations in the “perfect” terrace as well. These originate from the finite length of the trough, where its ends act as defects. These first calculations demonstrate that a parallel wave pattern is indeed a result of terrace disorder.

For a better understanding of particular features in the wave patterns observed in the experiments, we compare

$[dI/dV]_{\text{calc}}$ maps of varying terrace width and terrace disorder (Fig. 9). Terrace disorder has been modeled in the way described in the figure caption. Fig. 9 a, d, and g support the idea that a wave pattern perpendicular to the steps can only develop for larger terraces. The intensity of the parallel wave pattern increases with increasing disorder (Figs. 9a to c) and shows the same qualitative features as in the experiments. For example, some of the maxima in Fig. 9c are brighter than neighboring ones; some of them seem to be disconnected from neighboring maxima by deep minima, while between other maxima there are only little contrast variations. Fig. 9 c and i show that two bright protruding lines are seen instead of one for a larger terrace width. For the broadest disordered terrace (Fig. 9 h, i) the two wave patterns are thus superimposed. Minima in the two perpendicular patterns are displaced with respect to each other by up to half a wave length (Fig. 9i) as in the experiment. Many of the qualitative features of the experiments can thus be reproduced by the scattering theory, showing they result from terrace edge disorder.

2. Direct comparison with experiment

The calculations presented so far were meant to illustrate that the main physics is captured by the scattering theory and to emphasize the quality of the qualitative agreement between the scattering theory and experiment. Now, we go beyond these simple qualitative model calculations and use the actual surface-state dispersion for Ag(111) listed above and a terrace edge profile taken from experiment. The surface-state onset on a large terrace lies at $E_0 = -0.065$ eV; the effective mass is $m_{\text{eff}} = 0.4m_e$. These values lead to $\lambda_F = 7.38$ nm for the Fermi-wavelength on an infinite terrace. First, we calculate position dependent $[dI/dV]_{\text{calc}}$ spectra for a 7.9 nm wide terrace with varying phase shift and compare them to the experimental spectra for the broadest terrace in Fig. 2. The phase shift of the scatterers is chosen to best reproduce the Fabry-Perot type oscillations with the tip-sample bias, as shown in Fig. 10. The best agreement is reached with a phase shift of $\delta = (0.9 \pm 0.1)\pi$. Those spectra resemble the experimental ones with a shift in the apparent surface-state onset and a second peak in the unoccupied region. Note that in order to keep our fitting parameter to only the number δ , we do not include any energy dependence in the phase shift.

There is good agreement between the spectra calculated for the right half of the terrace (Fig. 10a), if spectrum number 14 showing no second maximum is taken as the central spectra, though it is measured 0.6 nm to the right of the geometrical center. This might be simply due to difficulties in determining the geometrical center of the terrace edges or may be due to the asymmetry of the reflection properties of ascending and descending step edges.¹⁷ The reflectivities of steps on this surface have been measured to be $r_{\text{desc}} = 0.72 - 2.91E/\text{eV}$ and

$r_{\text{asc}} = 0.48 - 2.86E/\text{eV}^{17}$ for the descending and the ascending step, respectively. Spectra 15, 16, and 17 are measured at a distance of 0.6 nm, 1.2 nm, and 1.8 nm from spectra 14 are compared to calculations performed at ‘0.7 nm’, ‘1.5 nm’, and ‘2.0 nm’ from the center of the terrace, respectively. In all cases, the peak at ≈ 20 meV lies at almost exactly the same energy and its relative intensity is well reproduced. The first peak lies also at approximately the correct energy. However, a sharp rise in the theoretical spectra (an artifact of the calculation procedure) makes a comparison difficult for the first peak. In both theory and experiment, the second peak is broader than the first peak, because the reflectivity and thus the lifetime of the resonance decreases with increasing energy.

In Fig. 10 the peaks are sharper and more intense in theory than in experiment. Several processes may explain this difference in sharpness and intensity. On the experimental side, the spectra show thermal and modulation voltage broadening. We simulate the modulation voltage averaging and temperature broadening by averaging the theoretical spectra (Fig. 10b). Indeed, this broadening makes the additional peak in the theory at ≈ -20 meV undetectable in the experiment and lowers the intensity of the peak at +20 meV. However, the theoretical peaks remain somewhat sharper, presumably from details associated with how the terrace edges are modeled. One may think that the “porous” nature of the walls may lead to a shorter lifetime, and hence a broader theory peak than what is observed experimentally. However, this appears not to be the case. Changing the number of atoms that make up the edge profile by 50% has a negligible effect on the widths of the peaks.

Discrepancies may result from not correctly modeling the energy dependence of the reflectivity by replacing the steps by point scatters: The peaks in dI/dV can be associated with Fabry-Pérot type resonance with an energy dependent reflectivity.²⁵ As a narrower resonance means a longer lifetime, and thus a greater reflectivity, we conclude that theory has an effective reflectivity which is larger than experiment. The calculation has an energy dependent reflectivity, but because the walls are built up from point scatterers, it is difficult to determine the reflectivity exactly in order to compare it directly with experimental results for a “perfect” terrace. With effort, a very close match could be made by making the phase shift energy dependent and possibly adding imaginary parts as well, but extremely accurate numerical agreement is not our goal here. Rather, we wish to understand what is responsible for the essential features of the data. A more accurate calculation than ours would also include changes to the surface-state band dispersion itself due to the terrace edges. Recall that our theory uses the surface-state dispersion of the free surface-states.

The dI/dV spectra to the left and to the right of the center differ in both experiment and theory as a result of an asymmetry in the disorder of the two terrace edges. However, for the experimental spectra to the left of the

center, the second peak shifts with position on the terrace. This is not recovered in the calculation (Fig. 10c). We attribute this difference to the fact that the spectra are calculated for a terrace that is some 10% smaller than the experimental terrace and that has a different shape in detail, on the one hand, and to the larger difference in reflectivity properties between a row of atoms and a descending step than a row of atoms and an ascending step, on the other hand. The asymmetry in scattering properties of the two steps that can not be captured by replacing them by two rows of equivalent atoms leads thus to the ‘off-center middle’ (noted earlier in this section) and to larger discrepancies on the half of the terrace that is closer to the descending step edge. Despite these deviations in detail, the scattering theory does satisfactorily reproduce the experimental spectra. Thus, we have calculated dI/dV maps for a particular terrace for a direct quantitative comparison of experiments to theory. We have chosen terrace ‘3’ of Fig. 4 due to the clear wave pattern observed. This terrace is also broad enough that changes to the surface-state on narrow terraces²⁵ are negligible.

The terrace walls are approximated by 54 atoms placed as close to the actual boundary as possible (Fig. 11a, white dots). Fig. 11 compares the $[dI/dV]_{\text{meas}}$ maps, computed from Eq. (2), of Fig. 4j and k at -20 mV, at -10 mV, and of Fig. 5c at +90 mV to the calculation. The qualitative agreement is excellent: A similar wave pattern is observed in the calculated spectra as in the experimental one, both in the occupied and the unoccupied region. Also the decrease in wavelength from -20 meV to -10 meV is reproduced in the calculation. The comparison of the $[dI/dV]_{\text{meas}}$ line scans through the center of the terraces (Fig. 11c) shows this good wavelength agreement for both -20 meV and -10 meV. The fourth maximum at -20 mV in Fig. 11c is simply not resolved in the experimental data. Only the relative intensities are partly recovered.

We have also simulated the broadest terrace ‘3’ in Fig. 7 for a more detailed comparison of theory with experiment for wavelength changes in the unoccupied region. Fig. 12 shows the comparison of simulation and experiment at 33, 26, and 17 mV. Unfortunately, the direct comparison is somewhat obstructed by an impurity, visible by enhancing the contrast in the topographic image (Fig. 12a) leading to a very particular wave pattern at -30 meV (Fig. 7b). At first sight, the comparison seems to be less favourable. The simulation shows two bright protruding lines close to the step edges separated by a dark stripe with little contrast variations. However, this reproduces the variation of intensity across the terrace in the experiments (from bright to weaker to bright). Despite the impurity the lines pass through the middle of the terrace agree well in wavelength in the upper part of

the image (Fig. 12d). Only a phase shift in the lower part is not recovered. Thus, again the major difference lies in intensity. This last example underlines the complexity of the evolved wave pattern and that it may depend quite sensitively on various details of the geometry.

IV. CONCLUSIONS

We have probed the LDOS of disordered terraces of varying width and observed oscillations *parallel* to the terraces with a wavelength in accordance with a free electron dispersion, and we have shown that these parallel oscillations arise naturally in scattering theory calculations for disordered terraces. The theory also captures important contrast variations with tip-sample voltage polarity. Thus, the wave patterns observed experimentally are a result of step disorder.

The complete pattern is a combination of Fabry-Pérot (surface-state) and disorder scattering effects along with surface reconstruction effects. The Fabry-Pérot effects are intrinsic in scattering theory, but the changes to the underlying surface-state band structure are not (in the theoretical model used here, which assumes a clean surface-state dispersion). As the scattering theory recovers all the qualitative features of the experiment and yields semi-quantitative agreement, the surface-state scattering effects dominate (at least for the wider terraces). Remaining differences are attributed to surface reconstruction effects. The semi-quantitative agreement in the simulation also shows that the cross-talk between the large terraces and their neighbors is negligible.

The terraces that the dI/dV maps have been calculated for are wide enough to allow us to use the surface-state band structure valid for infinitely broad terraces. In principle narrower terraces could be calculated within the same theory by using the appropriate dispersion relation for narrower terraces, which will in general be anisotropic and depend on terrace width.³⁰

As a future project, we suggest to locally investigate the reaction dependence on the vicinal surface and we expect local variation on the nanometer scale due to the reported variation of the LDOS.

V. ACKNOWLEDGEMENT

We acknowledge financial support by the Deutsche Forschungsgemeinschaft, NSF-9907949, NSF DMR-0227743 and the Packard Foundation. We are grateful for experimental support by K.-F. Braun, Ohio University, Athens.

¹ W. Shockley, Phys. Rev 56, 317 (1939).

² F. Forstmann, Z. Phys. 235, 69 (1970).

³ S.D. Kevan, R.H. Gaylord, Phys. Rev. B 36, 5809 (1987)).

⁴ P. Roos, E. Bertel, K.D. Rendulic, Chem. Phys. Lett. 232, 537 (1989).

⁵ P.O. Gartland, B.J. Slagsvold, Phys. Rev. B12, 4047 (1975).

⁶ P. Heimann, H. Neddermeyer, H.F. Roloff, J. Phys. C10, L17 (1977).

⁷ A. Zangwill, Physics at Surfaces, Ch. 4 (Cambridge Univ. Press, Cambridge, 1988).

⁸ J. Tersoff, D.R. Hamann, Phys. Rev. B31, 805 (1985).

⁹ M.F. Crommie, C.P. Lutz, D.M. Eigler, Nature (London) 363, 524 (1993).

¹⁰ M.F. Crommie, C.P. Lutz, D.M. Eigler, Science 262, 218 (1993).

¹¹ P. Avouris, I. Lyo, Science 264, 942 (1994).

¹² O. Sanchez, J.M. Garcia, P. Segovia, J. Alvarez, A.L. Vazquez de Parga, J.E. Ortega, M. Prietsch, R. Miranda, Phys. Rev. B52, 7894 (1995).

¹³ J.M. Garcia, O. Sanchez, P. Segovia, J.E. Ortega, J. Alvarez, A.L. Vazquez de Parga, R. Miranda, Appl. Phys. A 61, 609 (1995).

¹⁴ J.E. Ortega, S. Speller, A.R. Bachmann, A. Mascaraque, E.G. Michel, A. Närmann, A. Mugarza, A. Rubio, F.J. Himpsel, Phys. Rev. Lett. 84, 6110 (2000).

¹⁵ J. Li, W.D. Schneider, R. Berndt, Phys. Rev. B56, 7656 (1997).

¹⁶ J. Li, W.D. Schneider, R. Berndt, S. Crampin, Phys. Rev. Lett. 80, 3332 (1998).

¹⁷ O. Jeandupeux, L. Bürgi, A. Hirstein, H. Brune, K. Kern, Phys. Rev. B59, 15926 (1999).

¹⁸ L. Bürgi, O. Jeandupeux, H. Brune, K. Kern, Phys. Rev. Lett. 82, 4516 (1999).

¹⁹ P.T. Sprunger, L. Petersen, E.W. Plummer, E. Lægsgaard, F. Besenbacher, Science 275, 1764 (1997).

²⁰ L. Bürgi, L. Petersen, H. Brune, K. Kern, Surf. Sci. 447, L157 (2000).

²¹ J. Repp, F. Moresco, G. Meyer, K.-H. Rieder, P. Hyldgaard, M. Persson, Phys. Rev. Lett. 85, 2981 (2000).

²² N. Knorr, H. Brune, M. Epple, A. Hirstein, M.A. Schneider, K. Kern, Phys. Rev. 65, 115420 (2002).

²³ K. Morgenstern, K.-F. Braun, K.H. Rieder, Phys. Rev. Lett. 93, 056102 (2004).

²⁴ K. Morgenstern, F. Besenbacher, Phys. Rev. Lett. 87, 149603 (2001).

²⁵ K. Morgenstern, K.-F. Braun, K.-H. Rieder, Phys. Rev. Lett. 89, 226801 (2002).

²⁶ G. A. Fiete, E. J. Heller, Rev. Mod. Phys. 75, 933 (2003).

²⁷ G. A. Fiete, J. S. Hersch, E. J. Heller, H. C. Manoharan, C. P. Lutz and D. M. Eigler, Phys. Rev. Lett. 86, 2392 (2001).

²⁸ M.P. Everson, R.C. Jaklevic, W. Shen, J. Vac. Sci. Technol. A8, 3662 (1990).

²⁹ M. Hansmann, J.I. Pascual, G. Ceballos, H.-P. Rust, K. Horn, Phys. Rev. B 67, 121409(R) (2003).

³⁰ F. Baumberger, M. Hengsberger, M. Muntwiler, M. Shi, J. Krempasky, L. Patthey, J. Osterwalder and T. Greber, Phys. Rev. Lett. 92, 196805 (2004).

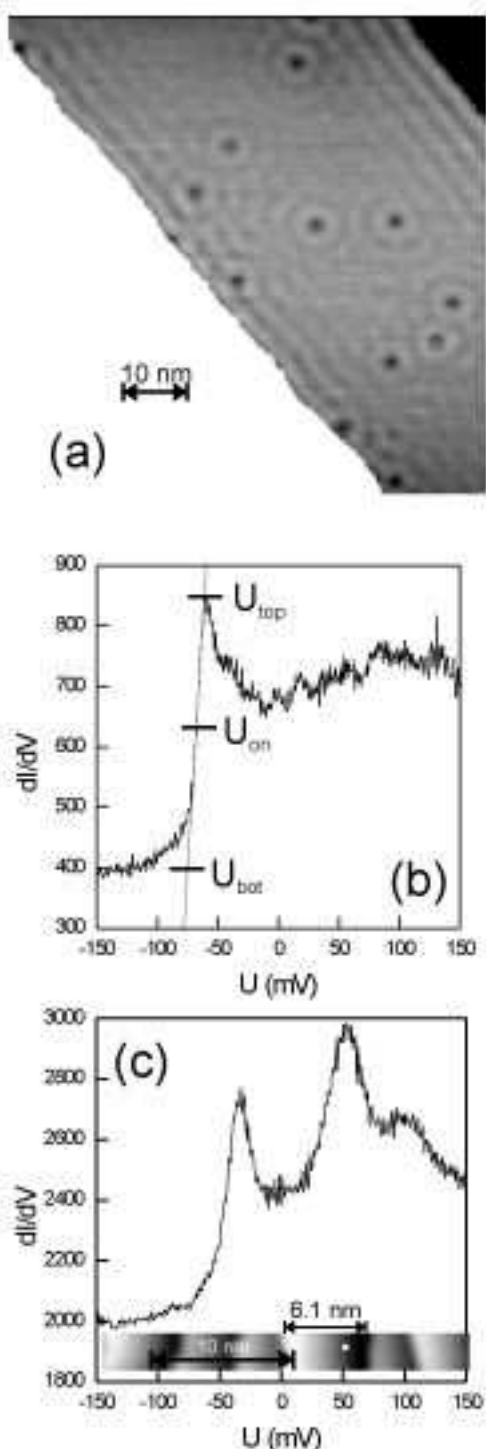


FIG. 1: (a) Real space STM image taken at 7 K showing spatial oscillations of electrons in the Ag(111) surface-state on a large terrace 51 nm in width. Circularly symmetric oscillations in the LDOS are seen around point impurities. The tip-sample voltage bias is $U_{bias}=32$ mV with a tunneling current $I_{tun}=0.43$ nA. (b) The surface state onset is indicated in the dI/dV spectrum on the large terrace shown in (a). Here $U_{on} = (U_{top} + U_{bot})/2$ is taken as the value of the onset. (c) The dI/dV spectrum on the edge of a narrow terrace of 6.1 nm width (indicated by a white dot on the inset STM image) shows two peaks in intensity. These peaks can be related to the onset of the lowest transverse mode of the terrace (first peak ≈ -50 mV) and the first excited transverse mode (second peak ≈ 50 mV). Here $U_{bias}=-137$ mV and $I_{tun}=0.34$ nA.

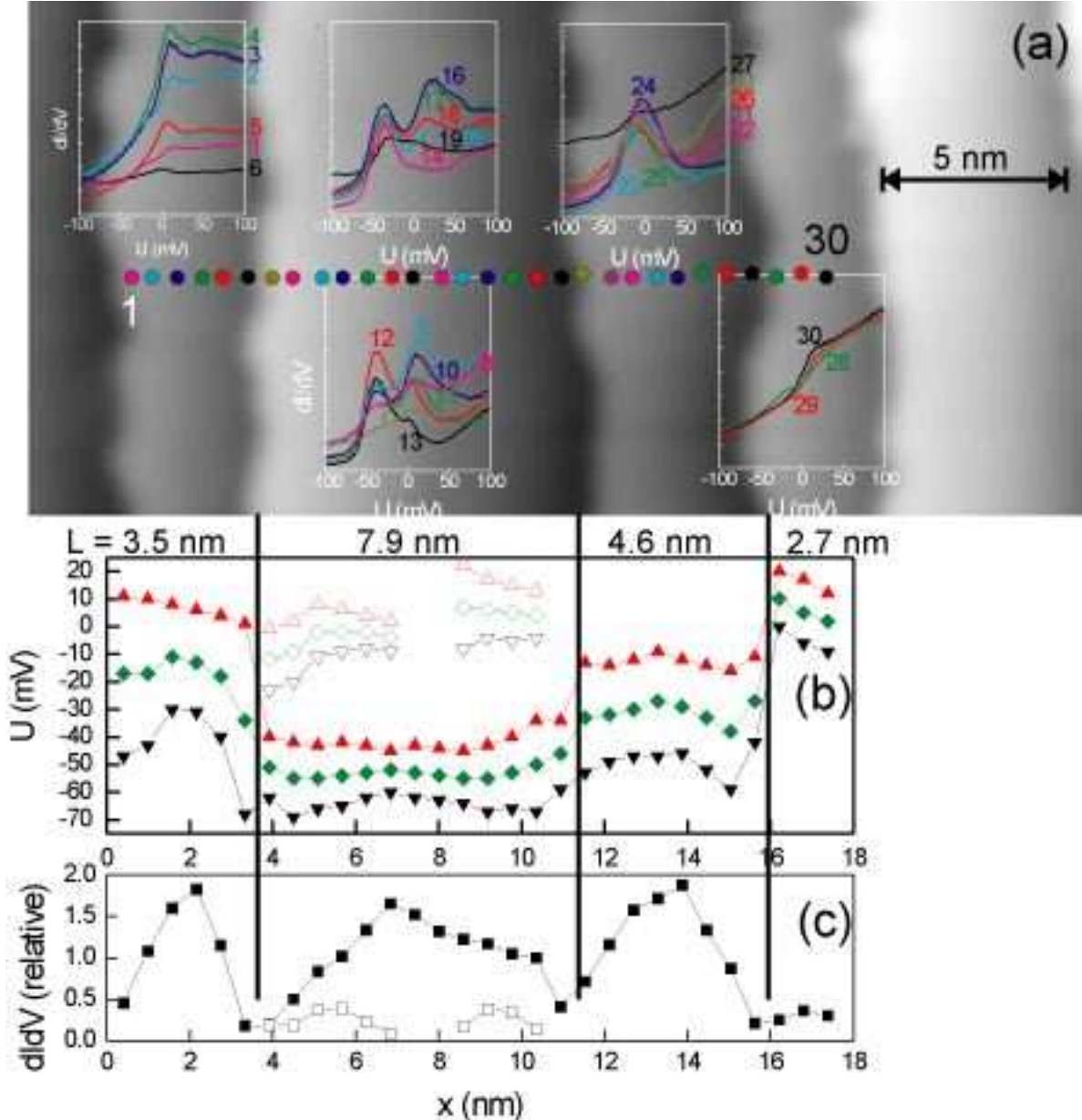


FIG. 2: (Color online.) Position dependent STS at different points across the width of different terraces showing the dependence of the surface-state onset and of the second maximum in dI/dV spectra on average terrace width and on position on the terrace. (a) The background grayscale image is a topographic image ($U_{bias}=-47$ mV, $I_{tun}=1.3$ nA) showing approximately 5 terraces with irregular, disordered edges. The average widths range from 2.7-7.9 nm. Superimposed on each terrace of the STM image is a set of inset STS data taken at various positions (indicated in color) across the terrace. The positions are numbered from left (1) to right (30). (b) Position of bottom (down triangle), top (up triangle), and middle (diamond) of first (filled symbols) and second (open symbols) peak in dI/dV spectra of (a). The second peak is only observed on the widest terrace (of width 7.9 nm) and is related to exciting the second transverse mode. Dark vertical lines indicate positions of the step (terrace) edges. (c) Relative intensity [i.e. $(dI/dV_{top} - dI/dV_{bot})/dI/dV_{bot}$] of the first peak (filled symbols) and the second peak (open symbols) for spectra of (a).

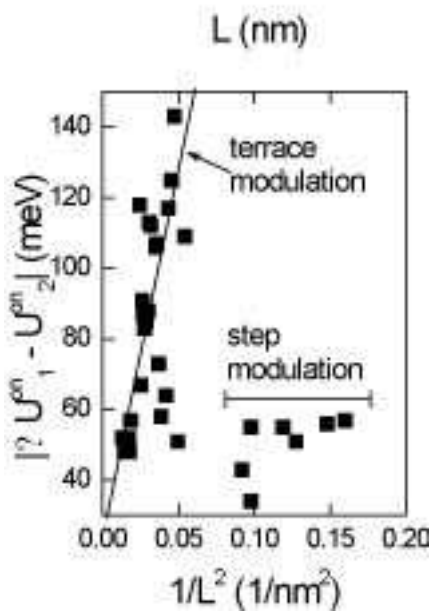


FIG. 3: Scaling of the relative position of the first and second maximum in dI/dV curves on small terraces vs. inverse terrace width squared. For terraces wider than $L \approx 4.3$ nm, $|U_1^{on} - U_2^{on}| \propto L^{-2}$ as shown by the linear fit, implying an interpretation consistent with the presence of transverse modes of the surface state. However, the effective mass determined, $m_{eff}^{terr} = (0.59 \pm 0.17) m_e$, deviates from the effective mass of electrons in the surface-state band where $m_{eff} = 0.4m_e$. On the other hand, terraces narrower than $L \approx 3.4$ nm do not scale linearly with L^{-2} , but instead show behavior consistent with step modulation.

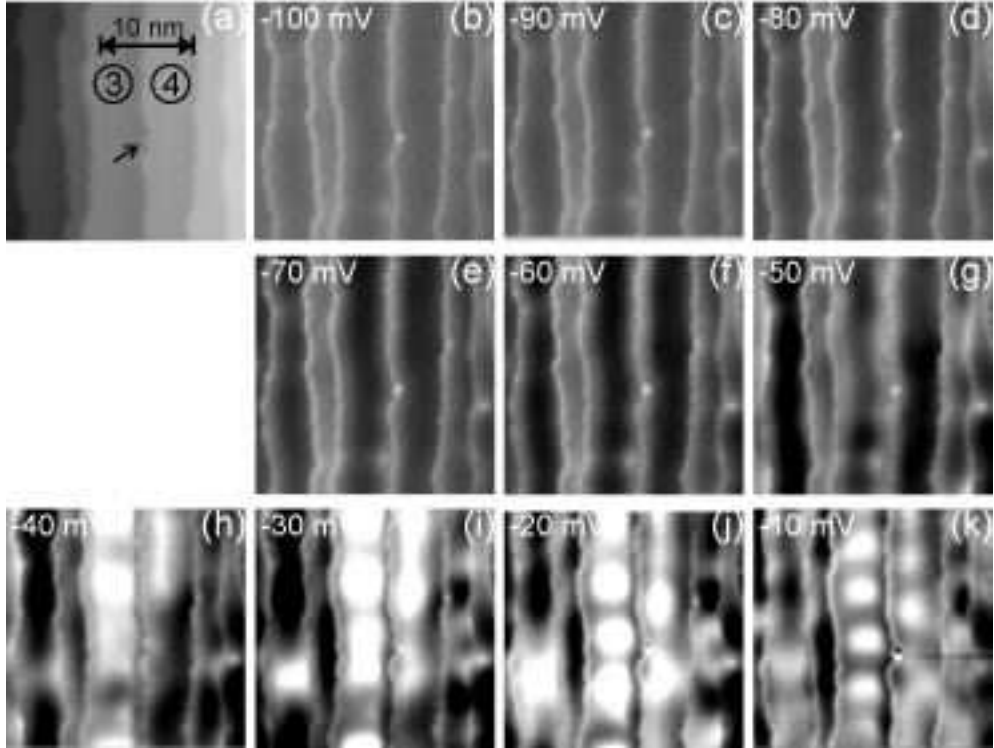


FIG. 4: dI/dV maps of Ag(111) terraces in the occupied region of the spectrum [negative tip-sample voltage bias, indicated in the upper left-hand corner of (b)-(k)]. The AC voltage modulation is $U_{mod} = 4$ mV and the frequency is $\nu_{mod} = 738.1$ Hz. (a) Topographic image ($U_{bias} = -100$ mV, $I_{tun} = 13$ nA). The two central terraces are labeled “3” and “4”. The arrow points to an impurity at step a edge between the two. (b)-(k) Show dI/dV maps for $U_{bias} = -100$ mV to -10 mV as indicated. Note the difference in wave patterns on the different terraces. In particular, the terraces “3” and “4” begin to develop oscillations in the LDOS parallel to the step edges over the range of tip-sample bias -40 meV $\lesssim U_{bias} \lesssim -10$ meV. The oscillations on terrace “3” are investigated in more detail in Fig. 11.

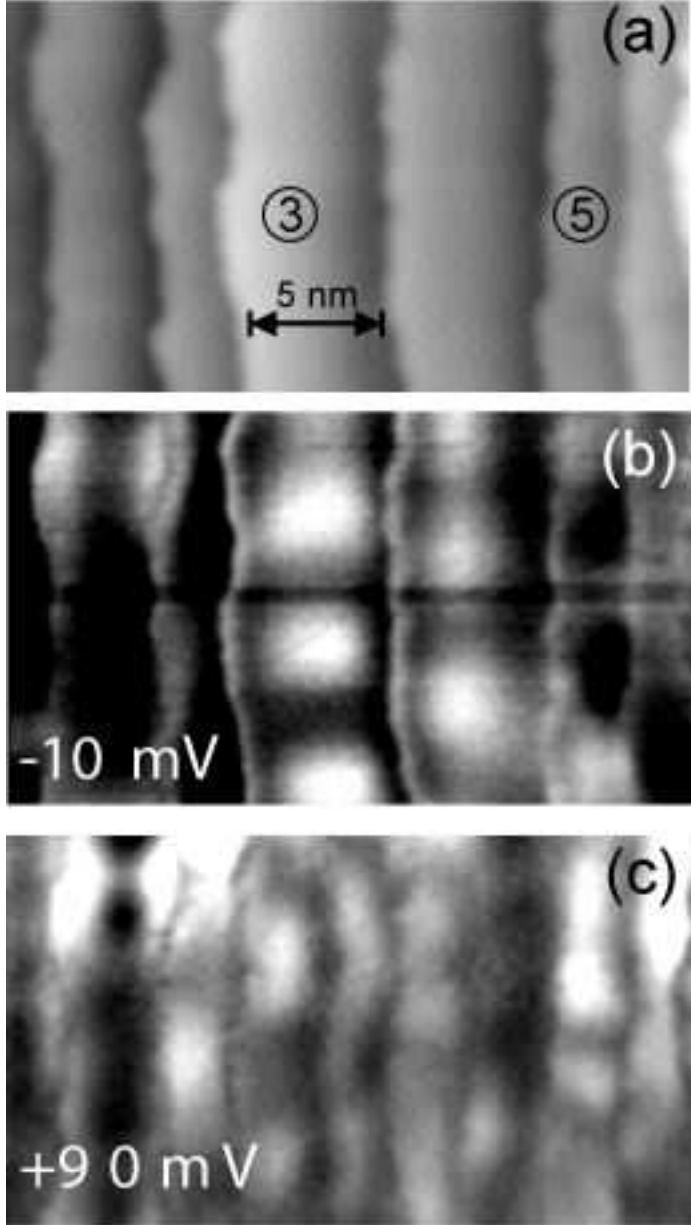


FIG. 5: Comparison of dI/dV maps for different tip-sample polarity with AC modulation parameters $U_{mod} = 4$ mV, $\nu_{mod} = 738.1$ Hz and $I_{tun} = 1.4$ nA. (a) Topographic image of approximately 6 irregular terraces. The terraces are the same as those shown in Fig. 4 (upper half). (b) dI/dV map at $U_{bias} = -10$ mV. (c) dI/dV map at $U_{bias} = 90$ mV. Note the parallel and perpendicular wave pattern on terrace “3” for negative and positive polarity, respectively. This change in the wave pattern can be understood with the scattering theory described in the text. See Fig. 11.

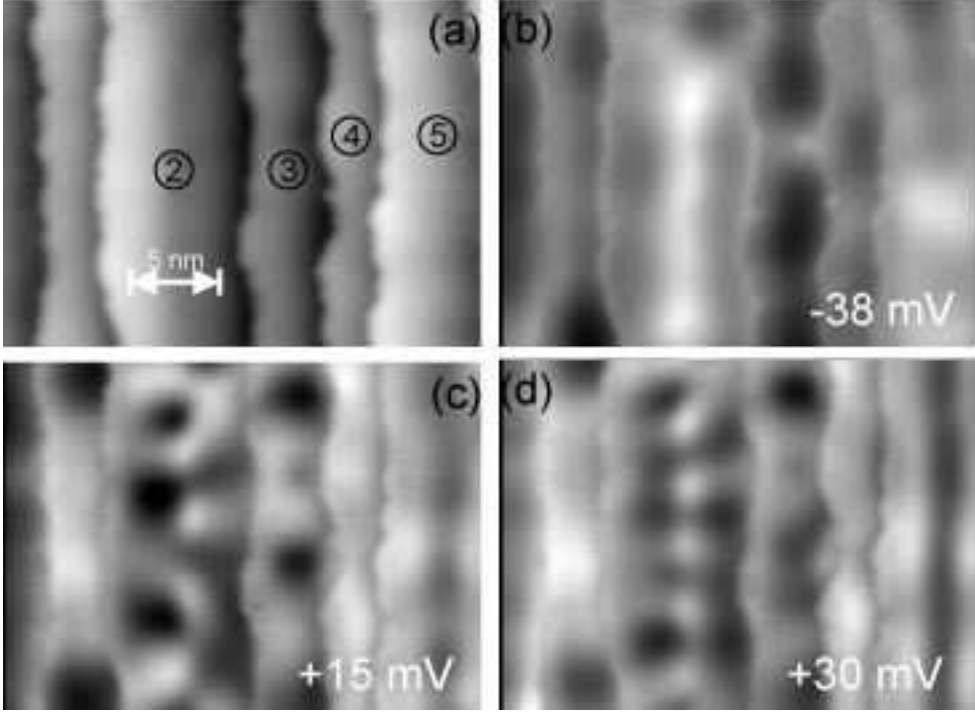


FIG. 6: Evolution of terrace wave patterns with U_{bias} . The terraces shown are different from the set shown in Figs. 4 and 5. The STM parameters are $U_{mod} = 4$ mV, $\nu_{mod} = 327.9$ Hz and $I_{tun}=1$ nA. (a) Topographic image taken at $U_{bias} = 15$ mV, $I_{tun}=1$ nA. Terraces “2”, “3”, “4”, and “5” develop distinct wave patterns with varying U_{bias} , indicating a clear dependence of wave pattern on both terrace edge disorder and terrace width. (b)-(d) dI/dV maps at -38 mV, $+15$ mV, and $+30$ mV. Note the interesting superposition of parallel and perpendicular wave patterns on terrace “2”.

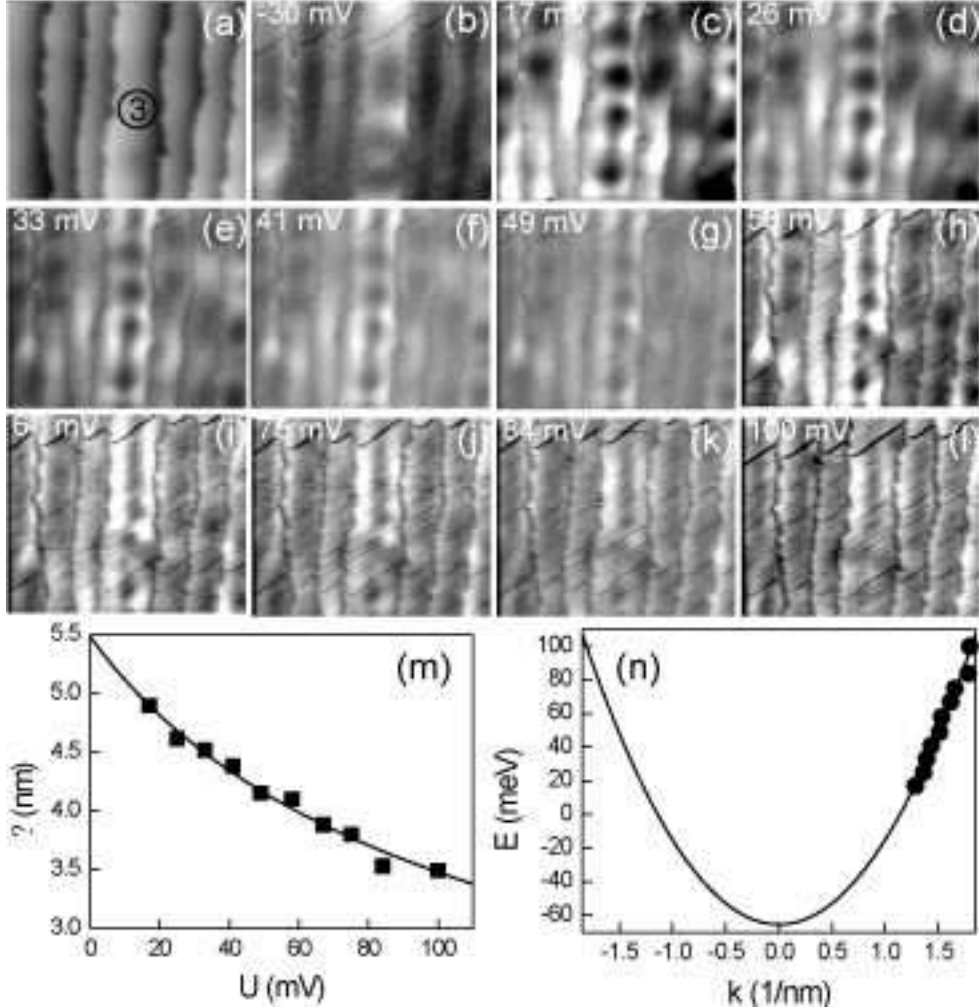


FIG. 7: Wavelength dependence of parallel wave patterns in unoccupied region of the energy spectrum (positive tip-sample bias). Compare with Fig. 4 which shows different terraces at negative U_{bias} . STM parameters are $U_{mod} = 8$ mV and $\nu_{mod} = 381.8$ Hz. (a) Topographic image (-30 mV, 0.39 nA). (b-l) dI/dV maps for $U_{bias} = 17$ mV to 100 mV and -30 mV as indicated. Black stripes (in h-l) are an artifact of the STM electronics and should be ignored. For better visibility (h)-(l) have four times the intensity contrast of (c)-(g). Note that there is a “contrast” reversal of the wave pattern of terrace “3” compared to those image shown in Fig. 4. This feature is also captured by the scattering theory. (See Fig. 12.) (m) Wavelength of standing waves on terrace “3” in (b) to (l) with square root fit. (See Sec. IIB in paragraph just below Eq. (1).) (n) Dispersion relation as deduced from the fit in (m).

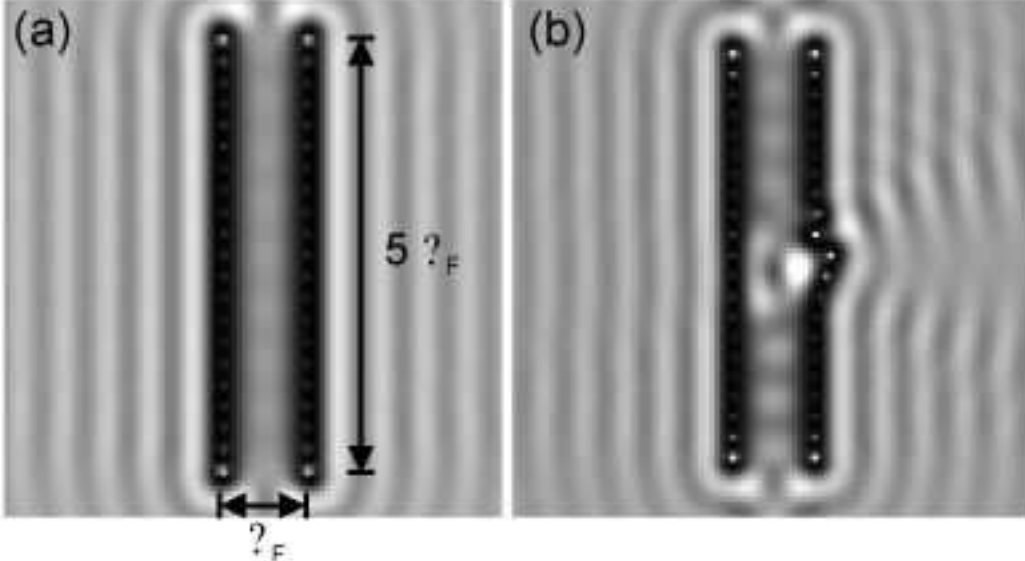


FIG. 8: Model scattering theory calculations illustrating creation of standing wave patterns in the LDOS parallel to the terrace edges when disorder is present. **Here “?”=“λ” due to a graphics error.** The terrace edges are modeled by rows of atoms. As long as the atoms are much closer together than the wavelength of the electrons in the surface state this is a good approximation. Shown are two $[dI/dV]_{\text{calc}}$ maps calculated with scattering theory for a terrace of length $5\lambda_F$ and width $\lambda_F/4$ with (a) no defect and (b) one defect. The introduction of a single point defect creates a strong variation in the LDOS parallel to the edges of the terrace. In both cases there are oscillations clearly visible perpendicular to the terraces edges outside the terrace.

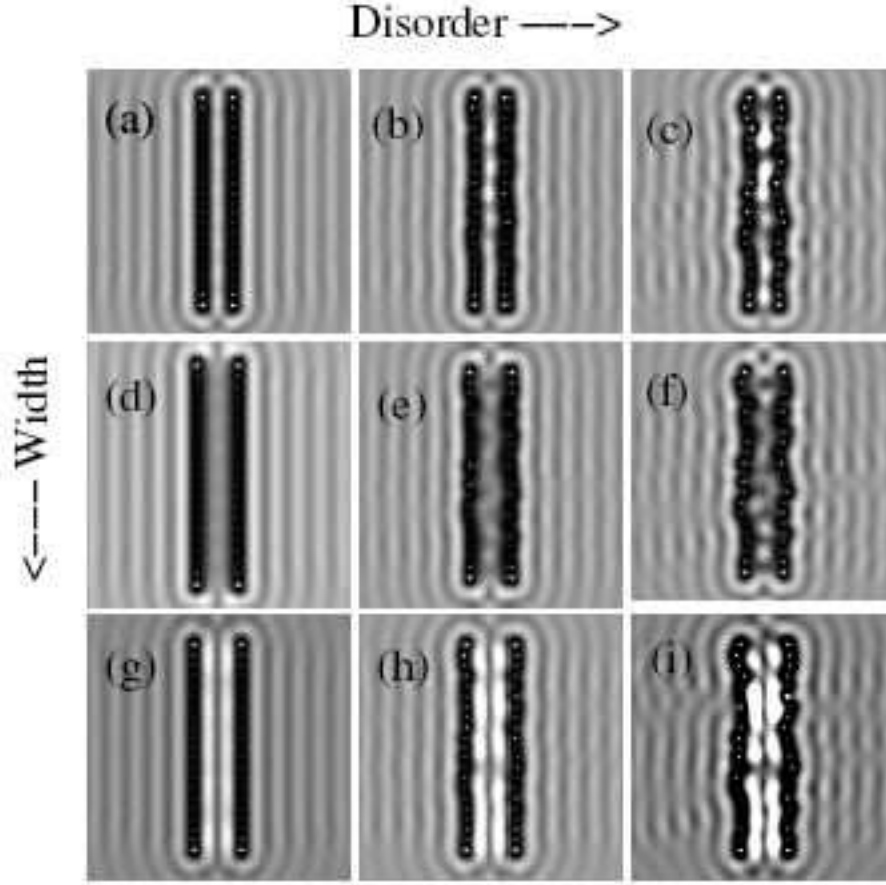


FIG. 9: Theoretical DI/dV maps for different width and disorder. Disorder is introduced manually by shifting the horizontal positions of the atoms that model the walls of the terrace. The characteristics of the disorder (such as whether or not the displacements are Gaussian distributed, what the RMS value of the fluctuations is, etc.) are unimportant for the qualitative study here. The maximum displacement of the “random” positions is: (a,d,g) 0, i.e., no disorder, (b,e,h) $\pm 8\%$ variation in width, and (c,f,i) $\pm 20\%$ variation in width. The average widths of the terraces are: (a,b,c) $0.8\lambda_F$, (d,e,f) λ_F , and (g,h,i) $1.2\lambda_F$. The features seen in (c) and (i) are qualitatively similar to those seen on terrace “3” in Fig. 4 at negative and positive voltage biases, respectively. See Fig. 11.

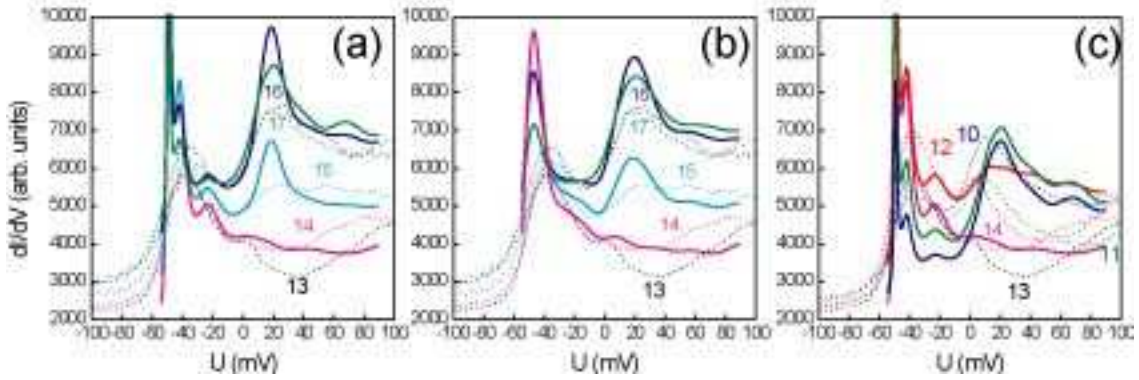


FIG. 10: (Color online.) Comparison of dI/dV spectra taken at different positions in the second terrace in Fig. 2a of width 7.9 nm. Solid lines: calculation with phase shift 0.9π in the surface-state scattering theory described in the text. Dotted lines: Experimental results. (a,c) Scattering calculation without thermal broadening. (b) same as (a), but theoretical curve is averaged over an energy window to simulate broadening due to thermal effects and modulation voltage. The quality of the agreement between experiment and theory in (b) is good considering the range of energy and the relative simplicity of the theory. The main disagreement occurs around $U \approx -50$ meV where the theory predicts a narrower and higher peak than is seen experimentally. This indicates the approximations used to model the terrace edge result in a more highly reflective edge at these energies than the actual edge in experiment.

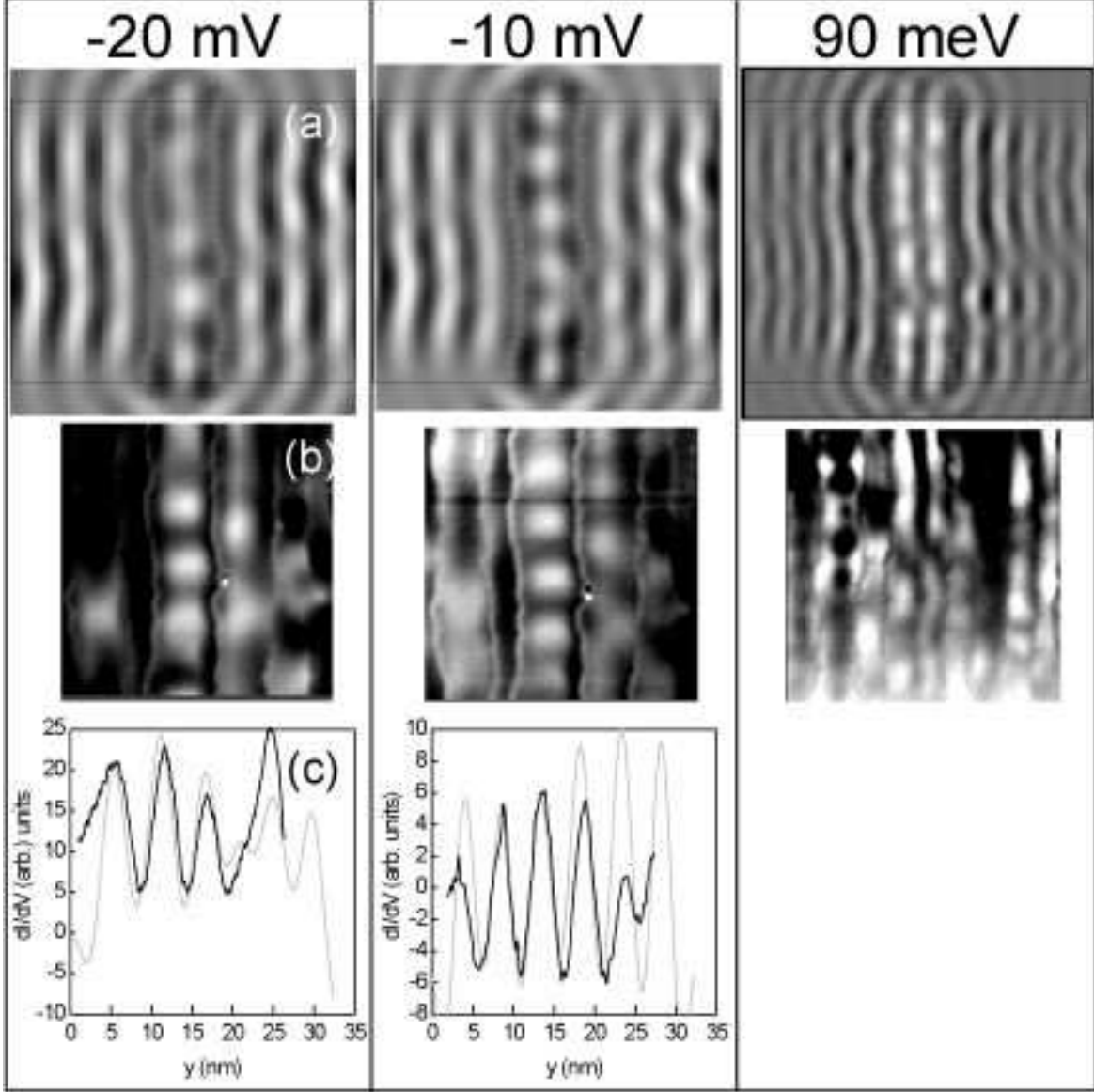


FIG. 11: Comparison of theoretical to experimental dI/dV maps for terrace “3” of Fig. 4 for bias voltages as indicated above the images. (a) Theoretical dI/dV maps computed using Eq. (2). (b) Experimental dI/dV maps. Note that the field of view in y -direction is larger in the theoretical maps than in the experimental maps as indicated in (a) by the faint horizontal lines near the top and bottom of the figures. The region in between these horizontal lines should be compared with the experimental figures in (b). (c) We show line scans through the middle of terrace “3”. Gray: theory. Black: experiment. The y -axis is different in the two spectra for better comparison.

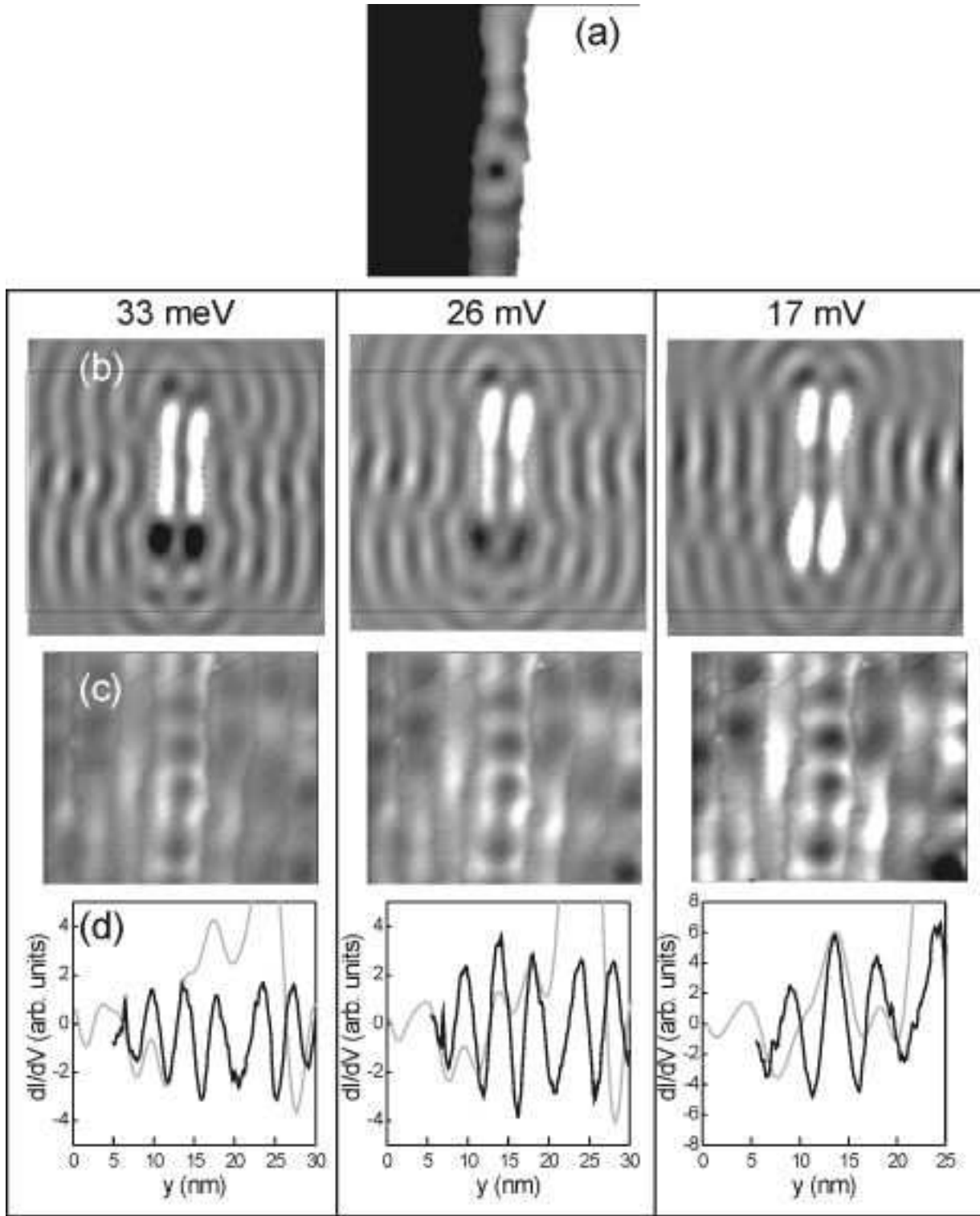


FIG. 12: Comparison of theoretical to experimental dI/dV map for unoccupied states (positive tip-sample bias). (a) Topography with enhanced contrast. Black dot on terrace indicates a point impurity. (b) Calculated dI/dV maps. As in Fig. 11 the region between the two faint horizontal lines should be compared with the experimental data in (c). (c) Experimental dI/dV maps of Fig. 7. (d) Line scans through middle of terrace. Gray: theory, Black: experiment.